

4D Thermomechanical Metamaterials for Soft Microrobotics

Qingxiang Ji^{a,b}, Johnny Moughames^b, Xueyan Chen^{a,b}, Guodong Fang^a, Juan J. Huaroto^b, Vincent Laude^b, Julio Andrés Iglesias Martínez^b, Gwenn Ulliac^b, Cédric Clévy^b, Philippe Lutz^b, Kanty Rabenorosoa^b, Valerian Guelpa^b, Arnaud Spangenberg^{c,d}, Jun Liang^{e,*}, Alexis Mosset^b, Muamer Kadic^{b,*}

^a National Key Laboratory of Science and Technology on Advanced Composites in Special Environments, Harbin Institute of Technology, Harbin, 150001, China

^b Institute FEMTO-ST, CNRS, University Bourgogne Franche-Comté, 25000 Besançon, France
Email address: muamer.kadic@univ-fcomte.fr

^c Université de Haute-Alsace, CNRS, IS2M UMR 7361, F-68100 Mulhouse, France

^d Université de Strasbourg, 4 Rue Blaise Pascal, 67081 Strasbourg, France

^e Institute of Advanced Structure Technology, Beijing Institute of Technology, Beijing, 100081, China
Email address: liangjun@bit.edu.cn

Abstract

Metamaterials have attracted wide scientific interest as promising candidates to break fundamental bounds on materials properties and to realize extraordinary devices such as invisibility cloaks and perfect flat lenses. Recently, the field has been extending to certain coupled physical phenomena where one physics acts as the driving force for another. Stimuli-responsive metamaterials, also referred to as 4D metamaterials, have been demonstrated for many combinations such as thermo-elasticity, magneto-optics or piezo-electricity. Herein, a soft ultra compact and accurate microrobot is described which can achieve controlled motion under thermal stimuli. The system consists of an organized assembly of two kinds of functional structures: a rotational element and a translational one. Both elements are designed basing upon the principle of the thermo-elastic bilayer plate that bends in response to temperature changes. Samples are fabricated using gray-tone lithography from a single polymer but with two different laser writing powers, thus making each part different in its thermal and mechanical behaviors. Excellent motion-controllable, reversible and stable features in a dry environment are verified by simulations and experiments, revealing broad application prospects for the designed soft micro actuators.

Introduction

Mechanical metamaterials are artificial materials with unusual effective mechanical properties that mainly result from structural design rather than from the properties of constituent materials [1–5]. Using additional physical controls, scientists have designed composite structures that not only go beyond the properties of their constituents but whose effective properties can even have a sign opposite to the latter [6–10]; they are categorized as stimuli-responsive metamaterials and are also known as 4D metamaterials [11–13]. Mechanical metamaterials have been designed to show superior mechanical properties in

various application fields. Taking a metamaterial approach toward the design of soft microrobots substantially increases the number of degrees of freedom in deformation and the available geometrical parameters [14–16]. Indeed, the complex behavior of highly deformable mechanical metamaterials can substantially enhance the performance of soft microrobots. Soft shape-matching materials based on mechanical metamaterials were proposed [17], with potential applications in soft robotics and wearable (medical) devices. Soft actuating materials are capable of changing their macroscopic shapes under external physical stimuli of the mechanical [18], the

electric [19–21], the photonic [22, 23], the thermotic [24, 25], the hygrometric [26–29], or the magnetic [30–32] type. Such stimuli-responsive materials play a key role in designing soft microrobots thanks to their brilliant shape recovery properties under applied stimuli that help the creation of programmable and accurate motion [33–35].

So far, actuating devices have been designed mainly using multilayered films or beams, exploiting the different physical response of two or more different materials. In the field of thermally driven metamaterials, actuators are usually realized by coupling two layers of materials with different thermal expansion coefficients and Young’s moduli [9, 36]. However, realizations of actuating metamaterials have to date only been reported for simple deformations like self-bending or been demonstrated for macroscopic structures, at the centimeter or millimeter scale. It remains a challenge to obtain more complex deformations under external stimuli, such as rotation and translation, by a more direct and practical fabrication approach directly at the microscale.

Here, we design thermally actuated elements that provide fundamental mechanical motions (rotation and translation) at the microscale, which are crucial deformations highly required by a microrobot performing in a controlled manner. Then we fabricate functional stacks combining the proposed elements. The fabrication of such complex bimaterial samples is realized using a single material system but locally varying laser exposure. The stacks produce accurate movement under an applied thermal stimulus and totally recover to the rest state when the external stimulus is switched off. The system supports accurate motional amplitudes, reversible response, and is well controlled by a simple thermo-mechanical process (thermal expansion) in a dry environment. We demonstrate the possibility of building a three-axis microrobot with a single material using single-step lithography and thus bring thermoelastic metamaterials for microrobots closer to real applications. Our proposed design is a highly promising basis paving the way for the next micro-nanorobotic generation.

Results and discussion

Design and fabrication of the metamaterial. We start by designing two elementary robotic unit cells

that produce either rotational or translational motion under a thermal stimulus (see Fig. 1). The elements can build up a functional stack and further assemble into a robotic arm with three orthogonal orientations (see Supplementary Figure 1 and Supplementary Concept Design). Such a robotic arm can realize multiple movements based on rotation and translation along each axis, which is vital to position a robotic tip in space (see Supplementary Movie 1). We illustrate the operating principle of the elements as follows: the bilayer beam expands and bends upon heating, due to the difference in thermal expansion properties, giving rise to a net translation (rotation) of the element (see Fig. 1b-c). The induced translational (rotational) motion of each element accumulates and enlarges the motional amplitudes at the end of the stack. By tailoring the translation (rotation) amplitudes for each axis, the robotic arm is capable of performing three-dimensional (3D) motion in response to an external thermal stimulus. In addition, the motional amplitude of the tip end is well controlled by temperature changes.

In this work, we use 3D gray-tone two-photon lithography to fabricate complex two-component metamaterials. It is far from trivial to print such structures with two different materials in a single step at the micro-scale. We note that the key to thermally responsive metamaterials primarily lies in the thermal expansion properties of the two different components. It was demonstrated in references [9, 37] that the coefficient of thermal expansion (CTE) does not only depend on the type of polymer used, but for a given monomer it also depends on the laser writing power during photo-polymerization. As a proof, we have fabricated bulk polymer cubes with different writing powers (side length $50 \mu\text{m}$, made from IP-Dip, Nanoscribe GmbH) and we have measured their CTEs. In the fabrication process, an average value of 20 mW is defined as the reference power. The actual power is given by the reference power times the power scaling factor, which is varied locally in the spirit of gray-tone lithography. We change the power scaling factor (and hence the exposure power) to fabricate different cubes (see Fig. 2a). During the measurement, we heat each polymer cube with a thermal gradient $\Delta T = 50 \text{ K}$ and capture images of the deformation. By using the public domain image pro-

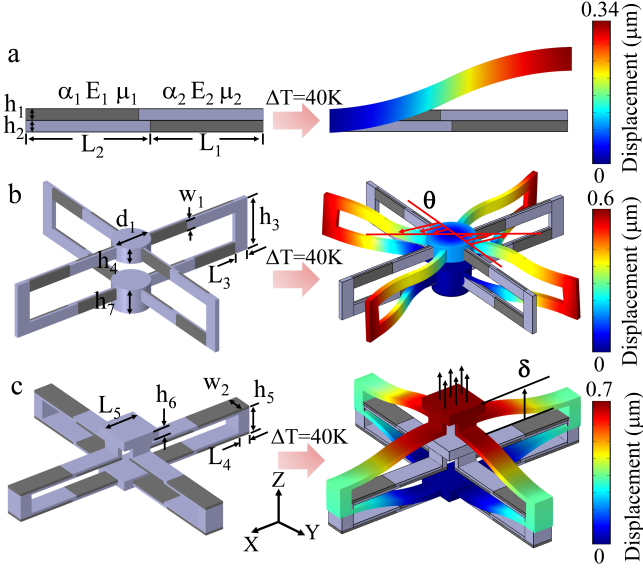


Fig. 1. Illustration of the operating principle of rotational and translational stages. (a) Bi-material beam and its deformation under a change in surrounding temperature of 40 K. (b-c) Operating principle of the translational and rotational elements, respectively. The component with higher (lower) CTE is depicted in blue (gray). The initial positions of the elements are outlined for visual comparison. The directions of rotation (translation) are indicated by red (black) arrows. For clarity, deformations in panel (a) and panels (b-c) are scaled by 10 times and 40 times, respectively. Key parameters marked in the panels are: $\alpha_1 = 3.84 \times 10^{-5} \text{ K}^{-1}$, $\alpha_2 = 4.67 \times 10^{-5} \text{ K}^{-1}$, $E_1 = 3.98 \text{ GPa}$, $E_2 = 3.9 \text{ GPa}$, $\mu_1 = \mu_2 = 0.4$, $h_1 = h_2 = 3 \mu\text{m}$, $h_3 = 54 \mu\text{m}$, $h_4 = 21 \mu\text{m}$, $h_5 = 36 \mu\text{m}$, $h_6 = 12 \mu\text{m}$, $h_7 = 33 \mu\text{m}$, $L_1 = 57 \mu\text{m}$, $L_2 = 63 \mu\text{m}$, $L_3 = 18 \mu\text{m}$, $L_4 = 15 \mu\text{m}$, $L_5 = 48 \mu\text{m}$, $w_1 = 15 \mu\text{m}$, $w_2 = 24 \mu\text{m}$, $d_1 = 48 \mu\text{m}$.

cessing software ImageJ, we proceed to convert each image to 8-bit format, then define edges and consequently convert the images to binary ones. Closing and filling algorithms are successively performed to obtain the internal areas defined by the edges (see Fig. 2f,g). Finally, based on the obtained areas measured in pixels, we estimate the CTE following

$$\alpha_L = \frac{A_f - A_b}{2A_b\Delta T} \quad (1)$$

where A_b and A_f are the areas obtained from images captured before and after heating, respectively. The correlation between the CTE and the laser exposure power is established in Fig. 2i. We observe that the CTE decreases approximately linearly with the laser exposure power.

The mechanical properties (here Young's modu-

lus E) for different laser powers are also obtained by measuring the aforementioned bulk polymer cuboid samples. We use Brillouin light scattering to measure the longitudinal elastic modulus from which we obtain Young's modulus (see Supplementary Figure 2 and Supplementary Mechanical Properties Measurement). We observe quasi-linear dependence of Young's modulus on the laser exposure power, as increasing laser power results in enhanced photopolymerization and therefore increased stiffness [37, 38]. It is noted that only the ratio E_1/E_2 actually enters into the effective deformation of bi-material beams [9].

As a proof of demonstration, we fabricate bi-layer beams with two components defined by two different power scaling factors and beams with a single component for comparison (see Supplementary Figure 3 and Supplementary Fabrication Technique). Observations show that the two-component beams deform and bend as the surrounding temperature changes, but also that they shrink during development, whereas the single-component beams are almost not influenced by temperature variations, demonstrating that the two components indeed have different properties. We thereby safely validate the fabrication strategy and demonstrate the possibility of printing a microrobot in only one step using a single photoresist and gray-tone lithography.

Based on the above laser writing strategy, we fabricate the metamaterials depicted in Fig. 1 using a single photoresist but two laser writing powers. We construct the less active component with a laser power 10 mW and the more active component with a laser power 9 mW. Clearly, a larger difference in selected power scaling factors would bring in larger motional amplitudes; however, it would also add more difficulties during fabrication and would specially lead to less repeatable motions for poorly exposed polymers. Here, we aim at designing a repeatable response and thus we must use the less damageable material. Poorly exposed polymer structures are indeed porous, they shrink a lot and they are thus not resistant to ambient conditions. With the chosen power scaling factors the fabricated samples show better mechanical stability and fewer imperfections. Optical and scanning electron microscopy (SEM) micrographs of selected fabricated stacks are

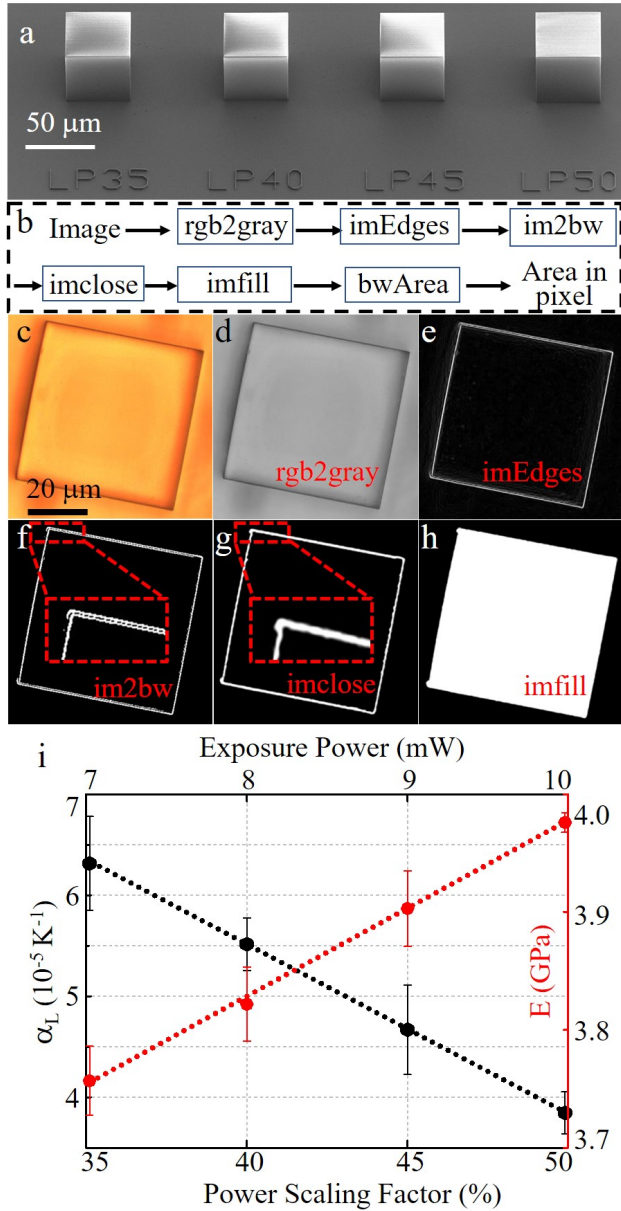


Fig. 2. CTE and Young's modulus measurement. (a) Bulk polymer cubes written by different laser power scaling factors. (b) Outline of the general process in ImageJ to obtain areas measured in pixels: the optical image of a polymer cube in panel (c) is first converted into 8-bit format in panel (d). Then an edge detection algorithm is applied and the image is converted into a binary image in panel (e). After applying closing algorithms in panel (f) and filling algorithms in panel (g), we finally obtain the internal area defined by these edges in panel (h). (i) The CTE versus laser exposure power is obtained by measuring areas before and after heating. The Young's modulus depicted in red is measured by Brillouin light scattering metrology. The bottom horizontal axis gives the power scaling factor whereas the top horizontal axis gives the actual power. We add black (red) error bars to indicate standard deviations of the calculated CTE (Young's modulus). The CTE decreases (Young's modulus increases) with the laser exposure power. Both variations are approximately linear.

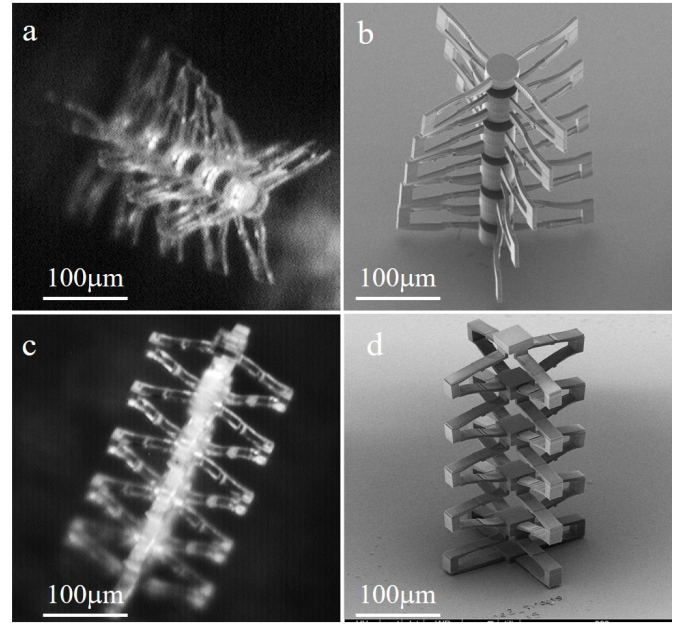


Fig. 3. Functional stacks fabricated by gray-tone lithography. (a) (c) Optical micrographs and (b) (d) SEM images. Each stack is composed of five elements. The samples are composed of two constituent components fabricated with a single photoresist but two different laser exposure powers. Differential shrinkage during development leads to pre-bending of the bi-layer beams, further leading to rotation (translation) of the stack shown in the panels.

shown in Fig. 3. We stress that the built components look alike in optical and electronic images, but that they are actually different in their thermal and mechanical properties. We notice the pre-bending of bi-material beams, which originates from different volume shrinkage during the development process. Within the linear regime, this pre-bending does not change the thermal operation. Instead, it directly evidences that the two components with different exposure powers are different in their thermal and mechanical properties. We can also notice the rotation (or translation) that results from pre-bending, in agreement with the designed operation principle.

Characterization of the thermally responsive behavior. To test the concept, we discuss the actuating performance of the functional stacks (see Supplementary Figure 4 and Supplementary Conceptual Testing). Upon electron beam heating (for about 10 seconds), the structures exhibit a thermal-mechanical response with corresponding motion. We wait for a given time (here 60 minutes) for the environment

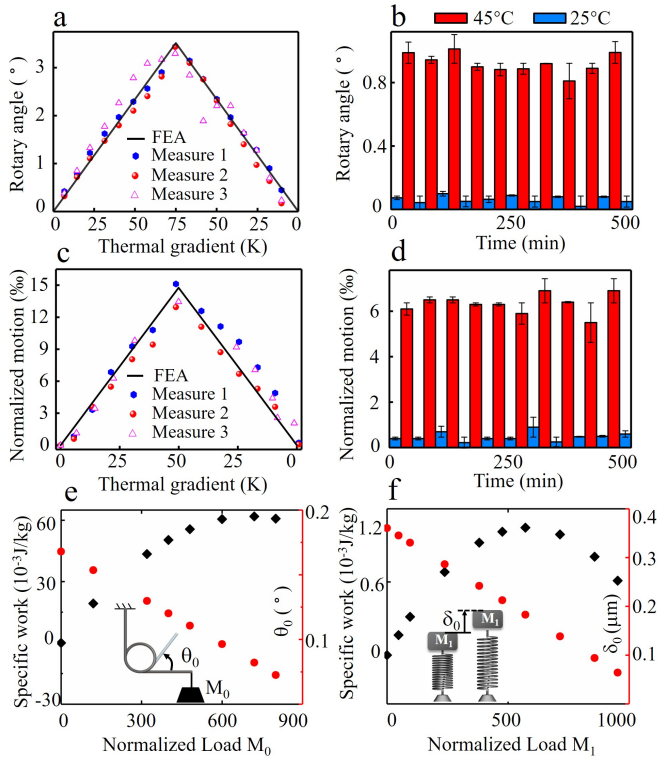


Fig. 4. Temperature-dependent measurement of the fabricated stacks. (a) (c) Dependence of motional amplitudes of the stacks with the thermal gradient for rotation and translation, respectively. The plots show a symmetric, linear and reversible amplitude response. (b) (d) Cyclic stability of the structures for rotation and translation, respectively, where temperatures are switched between 25°C (marked in blue) and 45°C (marked in red). The error bars (marked in black) indicate the difference between experimental and numerical results. Note that the translational displacements in panels (c-d) are normalized to the initial non-heated stack length in the z -direction. (e) (f) The specific work (i.e., the work normalized to the mass of the structure) and the actuation motion of the elements under thermal stimuli are plotted versus the normalized load and represented in analogy with Hooke's springs shown in the insets. Loads M_0 and M_1 have been normalized by the mass of the rotational element (2.5×10^{-10} kg) and translational element (2.1×10^{-10} kg), respectively. A linear relationship between displacements and external loads is observed in both cases, suggesting that the elastic limit is not reached.

and the samples to naturally cool back to the initial temperature. Note that such long cooling times are needed due to the absence of active cooling. When external heating is released, motion gradually decreases until the initial rest point is retrieved. Such an observation suggest that the thermal-driven behavior is sensitive and reversible.

In order to evaluate quantitatively the thermally

induced actuation mechanism, we conduct finite element analysis (FEA) and temperature-dependent measurements to check whether the structures behave exactly as designed. For FEA, we use the commercial software COMSOL Multiphysics. In the experiments, the structures are heated in an enclosed chamber with well controlled temperatures. We apply image cross-correlation analysis to obtain the temperature-induced displacement field and hence reveal the motion mechanism. Figure 4a,c summarizes the temperature-dependent measurement results, where temperatures are elevated gradually from 21.8°C to 96.4°C (with temperature difference around 75K) for the thermally induced rotation behavior and temperatures are elevated gradually from 21.8°C to 71.7°C (with temperature difference around 50K) for the thermally induced translation behavior, respectively. It is observed that the rotational and translational amplitudes increase linearly with the thermal gradient, in good agreement with FEA. Desired motional amplitudes can hence be accurately achieved by applying predefined temperature variations. Besides, motional amplitudes decrease to zero as the temperature returns to its initial value, revealing a well reversible performance. These results quantitatively demonstrate that the designed structures feature an accurate and reversible behavior under thermal stimuli. Movies of rotation (Supplementary Movie 2) and translation (Supplementary Movie 3) under thermal stimuli are available in the Supplementary information. We can observe minor differences between the measured results and the FEA results. The uncertainty mainly originates from the inaccuracy of the measured CTE and Young's moduli. Imperfections of the fabricated samples also add to these differences. For example, due to a drift during writing, the two layers in some of the bi-material beams may not be well connected, even to the extent of detaching.

To check the robustness of the thermally-driven operation, we test the functional stack under several heating-and-cooling cycles. Both the heating process and the cooling process last for 25 minutes during each cycle, ensuring that the system can reach its steady state. Hence, the full cycle time of a reversible switch is 50 minutes for the thermal cycling conditions used. As shown in Fig. 4b, the rotation angle

changes from around 0.08° to 0.92° as temperatures are switched from 25°C to 45°C . This actuation is reversible and repeatable upon several heating-and-cooling cycles, and the thermally-induced motional amplitudes are stable with small deterioration, which demonstrates a predictable long and stable working life. Similar relations of translational stacks are also observed in Fig. 4d. One may raise concerns regarding the small motion produced by the samples. In this work, the samples are fabricated to demonstrate extremely accurate and reversible operation, at the sacrifice of motional amplitudes. However, the observed motion is still comparable to what has been reported in the literatures for micro-structured thermally responsive metamaterials in a dry environment [9] and it has to be emphasized that actuation is remotely controlled and does not rely on an external mechanical actuation as is often the case. We investigated by numerical simulation the relationship between motional amplitudes and constructed parameters (see Supplementary Figure 5 and Supplementary Parameter Analysis). It is found that the amplitudes can be effectively adjusted by tuning structural and material parameters, or imposing larger temperature variations.

We finally estimate the potential torque (or force) that the designed structures can produce to move an object. The analysis of mechanical responses requires the correlation of the motional amplitude to an external load. Thereby, we use numerical calculations with the commercial software COMSOL Multiphysics. In our simulations, we consider a rotational (or translational) element with a torque (or force) applied to the sideways surface (or to the top end) in the opposite direction to the thermally induced displacement. A temperature elevation of 20 K is then imposed. Motional amplitudes are obtained versus increasing weight loading. The load-carrying capability is characterized by the applied load and by the specific work that the elements produce under the temperature elevation. The rotational (translational) elements work like Hooke's torsion (linear) springs by twisting (pushing) the end along its axis. Specifically, when a rotational (translational) element undergoes a temperature elevation, it exerts a torque (force) on external objects that is proportional to the angle (displacement), in analogy with a spring in

a twisted (compressed) state (see the insets in Fig. 4e,f). Note that the torsion (linear) spring strictly obeys Hooke's law, as the elastic limit is not reached in this work (see Supplementary Figures 6-7 and Supplementary Actuation Performance).

With increasing weight loading, the actuation angle (displacement) decreases linearly while the specific work first increases to the maximum value of $59 \times 10^{-3} \text{ J kg}^{-1}$ ($1.1 \times 10^{-3} \text{ J kg}^{-1}$) and then decreases gradually. Importantly, elements with a temperature elevation $\Delta T = 20\text{K}$ can offer a considerable actuation torque (or force) that is able to move roughly 1000 times their own weight (see Fig. 4e,f). The results are comparable with the characterization results in literature [34] in which, however, only contraction at the millimeter scale are demonstrated. Note that one can obtain larger actuation torque (or force) by simply imposing larger temperature variations or by adjusting construction parameters.

Conclusion

In summary, we have developed thermomechanical metamaterials that achieve elementary motions (rotation and translation) under thermal stimuli and can further assemble into a three-axis microrobot. The thermally driven behavior is obtained in a controlled manner and in a dry environment. The proposed metamaterials are fabricated using a single polymer but two different laser writing powers, thus making each part different in its thermal and mechanical properties. We verified that the designed compact metamaterials show accurate, stable, and reversible response through numerical simulations and experiments. Their operation can be easily and accurately controlled by external thermal sources, with great potential in microrobotics and other related domains.

Methods

Samples design. The thermally actuated structures are based on bilayer beams, utilizing the different thermal and mechanical properties of two different layers. To obtain the maximum thermally induced motion and hence the best actuation performance, optimization was conducted on the bilayer beams. Instead of a simple single bimaterial beam, a S-shaped pattern was chosen. For a single bilayer beam under a thermal stimulus, both axial and tangential

movements are induced. The end of a bilayer beam will be tilted (see Supplementary Figure 8a). Such a tilt angle at the end of the bilayer beams significantly reduces the effective motional amplitude of the whole structure. If two bilayer beams with inverted layer compositions are connected to form a S-shaped beam, the tilt angle at the end of the second beam is compensated for (see Supplementary Figure 8b and Supplementary Sample Design) [39]. An overlap part was added to connect the two inverted bilayer beams, making the structures mechanically more robust. Besides, the overlap part largely facilitates the fabrication process.

Samples fabrication. The rotational and translational stacks were both assembled in the z -direction by 5 elements. Samples were fabricated using a negative tone photoresist (IP-Dip, Nanoscribe GmbH) and a commercial 3D gray-tone two-photon lithography system (Photonics Professional, Nanoscribe GmbH). A drop of resin was deposited on a fused silica substrate with dimensions $25 \times 25 \times 0.7 \text{ mm}^3$ and photopolymerized with a femtosecond laser operating at $\lambda=780 \text{ nm}$. After printing, the sample was developed for 20 min in Propylene glycol methyl ether acetate (PGMEA) solution to remove the unexposed photoresist and rinsed for 3 min in Isopropyl alcohol (IPA) to clear the developer. In the fabrication process, the more active component was first fabricated with a laser power 9 mW. Then the laser was drifted and another component was fabricated with a laser power 10 mW. A Galvanometric scan speed of 10 mm s^{-1} was used for the whole fabrication process. Key material properties and geometry sizes of the samples are listed in Fig. 1.

Temperature-dependent characterization. During the measurements, the samples were placed on a flat heater within an encapsulated chamber. In this manner, the samples, as well as the air within the chamber, were heated by the heater. After a certain time (here we chose 25 minutes), we assumed that the system reached its steady state and that the sample temperature was uniform and stable which was actually equal to the surrounding air temperature. The heating processes were controlled by a commercial Linkam system, ranging from 25°C to 100°C . For accuracy, we placed a calibrated thermo-sensor at the

sample location and recorded live temperatures during each heating process. The chamber had a glass window on the top end, allowing for optical access and imaging by an optical microscope. Images were acquired using a single microscope lens (Achromplan 20 \times with a numerical aperture $NA = 0.4$) via a charge-coupled-device (CCD) camera. The samples were moved with respect to the microscope by manually moving the entire chamber using a translation stage. For each sample, We observed them for at least three times.

Data availability

The data that support the findings of this study are available from the corresponding authors on reasonable request. Source data are provided with this paper.

References

- [1] B. Florijn, C. Coulais, M. van Hecke, Programmable mechanical metamaterials, *Physical Review Letters* 113 (17) (2014) 175503.
- [2] J. Christensen, M. Kadic, O. Kraft, M. Wegener, Vibrant times for mechanical metamaterials, *MRS Communications* 5 (3) (2015) 453–462.
- [3] G. W. Milton, *The Theory of Composites*, Cambridge Monographs on Applied and Computational Mathematics, Cambridge University Press, 2002. doi:10.1017/CBO9780511613357.
- [4] M. Kadic, G. W. Milton, M. van Hecke, M. Wegener, 3D metamaterials, *Nature Reviews Physics* 1 (3) (2019) 198–210.
- [5] F. Zangeneh-Nejad, D. L. Sounas, A. Alù, R. Fleury, Analogue computing with metamaterials, *Nature Reviews Materials* (2020) 1–19.
- [6] R. Fleury, D. L. Sounas, C. F. Sieck, M. R. Haberman, A. Alù, Sound isolation and giant linear nonreciprocity in a compact acoustic circulator, *Science* 343 (6170) (2014) 516–519.
- [7] M. Kadic, R. Schittny, T. Bückmann, C. Kern, M. Wegener, Hall-effect sign inversion in a realizable 3D metamaterial, *Physical Review X* 5 (2) (2015) 021030.
- [8] T. Koschny, C. M. Soukoulis, M. Wegener, Metamaterials in microwaves, optics, mechanics, thermodynamics, and transport, *Journal of Optics* 19 (8) (2017) 084005.
- [9] J. Qu, M. Kadic, A. Naber, M. Wegener, Micro-structured two-component 3D metamaterials with negative thermal-expansion coefficient from positive constituents, *Scientific Reports* 7 (2017) 40643.

- [10] C. A. Spiegel, M. Hippler, A. Münchinger, M. Bastmeyer, C. Barner-Kowollik, M. Wegener, E. Blasco, 4D printing at the microscale, *Advanced Functional Materials* (2019) 1907615.
- [11] M. Hippler, E. Blasco, J. Qu, M. Tanaka, C. Barner-Kowollik, M. Wegener, M. Bastmeyer, Controlling the shape of 3D microstructures by temperature and light, *Nature Communications* 10 (1) (2019) 1–8.
- [12] M. Hippler, E. D. Lemma, S. Bertels, E. Blasco, C. Barner-Kowollik, M. Wegener, M. Bastmeyer, 3D scaffolds to study basic cell biology, *Advanced Materials* 31 (26) (2019) 1808110.
- [13] M. Gernhardt, E. Blasco, M. Hippler, J. Blinco, M. Bastmeyer, M. Wegener, H. Frisch, C. Barner-Kowollik, Tailoring the mechanical properties of 3D microstructures using visible light post-manufacturing, *Advanced Materials* 31 (30) (2019) 1901269.
- [14] C. Coulais, D. Sounas, A. Alù, Static non-reciprocity in mechanical metamaterials, *Nature* 542 (7642) (2017) 461–464.
- [15] M. Brandenburger, X. Locsin, E. Lerner, C. Coulais, Non-reciprocal robotic metamaterials, *Nature Communications* 10 (1) (2019) 1–8.
- [16] A. Rafsanjani, K. Bertoldi, A. R. Studart, Programming soft robots with flexible mechanical metamaterials, *arXiv preprint arXiv:1906.00306* (2019).
- [17] M. Mirzaali, S. Janbaz, M. Strano, L. Vergani, A. A. Zadpoor, Shape-matching soft mechanical metamaterials, *Scientific Reports* 8 (1) (2018) 1–7.
- [18] M. Hippler, K. Weißenbruch, K. Richler, E. D. Lemma, M. Nakahata, B. Richter, C. Barner-Kowollik, Y. Takashima, A. Harada, E. Blasco, et al., Mechanical stimulation of single cells by reversible host-guest interactions in 3D microscaffolds, *Science Advances* 6 (39) (2020) eabc2648.
- [19] E. Acome, S. Mitchell, T. Morrissey, M. Emmett, C. Benjamin, M. King, M. Radakovitz, C. Keplinger, Hydraulically amplified self-healing electrostatic actuators with muscle-like performance, *Science* 359 (6371) (2018) 61–65.
- [20] M. Amjadi, M. Sitti, Self-sensing paper actuators based on graphite–carbon nanotube hybrid films, *Advanced Science* 5 (7) (2018) 1800239.
- [21] Z. Liu, S. Fang, F. Moura, J. Ding, N. Jiang, J. Di, M. Zhang, X. Lepró, D. Galvão, C. Haines, et al., Hierarchically buckled sheath-core fibers for superelastic electronics, sensors, and muscles, *Science* 349 (6246) (2015) 400–404.
- [22] Q. Shi, J. Li, C. Hou, Y. Shao, Q. Zhang, Y. Li, H. Wang, A remote controllable fiber-type near-infrared light-responsive actuator, *Chemical Communications* 53 (81) (2017) 11118–11121.
- [23] D.-D. Han, Y.-L. Zhang, J.-N. Ma, Y.-Q. Liu, B. Han, H.-B. Sun, Light-mediated manufacture and manipulation of actuators, *Advanced Materials* 28 (38) (2016) 8328–8343.
- [24] C. S. Haines, M. D. Lima, N. Li, G. M. Spinks, J. Foroughi, J. D. Madden, S. H. Kim, S. Fang, M. J. De Andrade, F. Göktepe, et al., Artificial muscles from fishing line and sewing thread, *Science* 343 (6173) (2014) 868–872.
- [25] S. M. Chin, C. V. Synatschke, S. Liu, R. J. Nap, N. A. Sather, Q. Wang, Z. Álvarez, A. N. Edelbrock, T. Fyrner, L. C. Palmer, et al., Covalent-supramolecular hybrid polymers as muscle-inspired anisotropic actuators, *Nature communications* 9 (1) (2018) 1–11.
- [26] D.-D. Han, Y.-L. Zhang, H.-B. Jiang, H. Xia, J. Feng, Q.-D. Chen, H.-L. Xu, H.-B. Sun, Moisture-responsive graphene paper prepared by self-controlled photoreduction, *Advanced Materials* 27 (2) (2015) 332–338.
- [27] R. Castaldo, G. C. Lama, P. Aprea, G. Gentile, V. Ambrogi, M. Lavorgna, P. Cerruti, Humidity-driven mechanical and electrical response of graphene/cloisite hybrid films, *Advanced Functional Materials* 29 (14) (2019) 1807744.
- [28] B. Shin, J. Ha, M. Lee, K. Park, G. H. Park, T. H. Choi, K.-J. Cho, H.-Y. Kim, Hygrobot: A self-locomotive ratcheted actuator powered by environmental humidity, *Science Robotics* 3 (14) (2018).
- [29] S.-W. Lee, J. H. Prosser, P. K. Purohit, D. Lee, Bioinspired hygromorphic actuator exhibiting controlled locomotion, *ACS Macro Letters* 2 (11) (2013) 960–965.
- [30] S. Tottori, L. Zhang, F. Qiu, K. K. Krawczyk, A. Franco-Obregón, B. J. Nelson, Magnetic helical micromachines: fabrication, controlled swimming, and cargo transport, *Advanced Materials* 24 (6) (2012) 811–816.
- [31] K. Li, T.-H. Chang, Q. Xie, Y. Cheng, H. Yang, J. Chen, P.-Y. Chen, Tunable magnetic response in 2d materials via reversible intercalation of paramagnetic ions, *Advanced Electronic Materials* 5 (6) (2019) 1900040.
- [32] V. Magdanz, S. Sanchez, O. G. Schmidt, Development of a sperm-flagella driven micro-bio-robot, *Advanced Materials* 25 (45) (2013) 6581–6588.
- [33] J. Wang, W. Gao, Nano/microscale motors: biomedical opportunities and challenges, *ACS nano* 6 (7) (2012) 5745–5751.
- [34] A. Kotikian, R. L. Truby, J. W. Boley, T. J. White, J. A. Lewis, 3d printing of liquid crystal elastomeric actuators with spatially programmed nematic order, *Advanced Materials* 30 (10) (2018) 1706164.
- [35] T.-Y. Huang, H.-W. Huang, D. Jin, Q. Chen, J. Huang, L. Zhang, H. Duan, Four-dimensional micro-building blocks, *Science Advances* 6 (3) (2020) eaav8219.
- [36] W. Jiang, D. Niu, H. Liu, C. Wang, T. Zhao, L. Yin, Y. Shi, B. Chen, Y. Ding, B. Lu, Photoresponsive soft-robotic platform: biomimetic fabrication and remote actuation, *Advanced Functional Materials* 24 (48) (2014) 7598–7604.
- [37] J. Rys, S. Steenhusen, C. Schumacher, C. Cronauer, C. Daraio, Locally addressable material properties in 3D micro-architectures, *Extreme Mechanics Letters* 28 (2019) 31–36.
- [38] E. D. Lemma, F. Rizzi, T. Dattoma, B. Spagnolo, L. Sileo,

A. Quattieri, M. De Vittorio, F. Pisanello, Mechanical properties tunability of three-dimensional polymeric structures in two-photon lithography, *IEEE transactions on nanotechnology* 16 (1) (2016) 23–31.

[39] K. Jia, S. Pal, H. Xie, An electrothermal tip–tilt–piston micromirror based on folded dual S-shaped bimorphs, *Journal of Microelectromechanical systems* 18 (5) (2009) 1004–1015.

Acknowledgments

This work was supported by the EIPHI Graduate School [grant number ANR-17-EURE-0002], the French Investissements d’Avenir program, project ISITEBFC [grant number ANR-15-IDEX-03], and the National Natural Science Foundation of China [grant numbers 11732002 and 11672089]. This work was supported by the french RENATECH network and its FEMTO-ST technological facility.

Author contributions

Qingxiang Ji and Muamer Kadic conceived the idea. Qingxiang Ji, Xueyan Chen and Julio Andrés Iglesias performed numerical simulations. Johnny Moughames and Gwenn Ulliac fabricated the samples and obtained optical and SEM images. Qingxiang Ji, Julio Andrés Iglesias, Juan J. Huaroto and Alexis Mosset designed and implemented the experiments. Qingxiang Ji, Guodong Fang, Juan J. Huaroto, Vincent Laude, Valerian Guelpa, Arnaud Spangenberg, Alexis Mosset and Muamer Kadic analysed the data and discussed the results. Qingxiang Ji, Guodong Fang, Vincent Laude, Cédric Clévy, Philippe Lutz, Kanty Rabenorosa, Arnaud Spangenberg, Jun Liang and Muamer Kadic prepared the manuscript. Muamer Kadic and Jun Liang supervised the overall project. All the authors contributed to the discussion and to finalizing the manuscript.

Competing interests

The authors declare no competing interests.

Additional information

Supplementary information is available from the corresponding author.

Correspondence and requests for materials should be addressed to Muamer Kadic.

Figure 1. **Illustration of the operating principle of rotational and translational stages.** (a) Bi-material beam and its deformation under a change in surrounding temperature of 40 K. (b-c) Operating principle of the translational and rotational elements, respectively. The component with higher (lower) CTE is depicted in blue (gray). The initial positions of the elements are outlined for visual comparison. The directions of rotation (translation) are indicated by red (black) arrows. For clarity, deformations in panel (a) and panels (b-c) are scaled by 10 times and 40 times, respectively. Key parameters marked in the panels are: $\alpha_1 = 3.84 \times 10^{-5} \text{ K}^{-1}$, $\alpha_2 = 4.67 \times 10^{-5} \text{ K}^{-1}$, $E_1 = 3.98 \text{ GPa}$, $E_2 = 3.9 \text{ GPa}$, $\mu_1 = \mu_2 = 0.4$, $h_1 = h_2 = 3 \text{ }\mu\text{m}$, $h_3 = 54 \text{ }\mu\text{m}$, $h_4 = 21 \text{ }\mu\text{m}$, $h_5 = 36 \text{ }\mu\text{m}$, $h_6 = 12 \text{ }\mu\text{m}$, $h_7 = 33 \text{ }\mu\text{m}$, $L_1 = 57 \text{ }\mu\text{m}$, $L_2 = 63 \text{ }\mu\text{m}$, $L_3 = 18 \text{ }\mu\text{m}$, $L_4 = 15 \text{ }\mu\text{m}$, $L_5 = 48 \text{ }\mu\text{m}$, $w_1 = 15 \text{ }\mu\text{m}$, $w_2 = 24 \text{ }\mu\text{m}$, $d_1 = 48 \text{ }\mu\text{m}$.

Figure 2. **CTE and Young’s modulus measurement.** (a) Bulk polymer cubes written by different laser power scaling factors. (b) Outline of the general process in ImageJ to obtain areas measured in pixels: the optical image of a polymer cube in panel (c) is first converted into 8-bit format in panel (d). Then an edge detection algorithm is applied and the image is converted into a binary image in panel (e). After applying closing algorithms in panel (f) and filling algorithms in panel (g), we finally obtain the internal area defined by these edges in panel (h). (i) The CTE versus laser exposure power is obtained by measuring areas before and after heating. The Young’s modulus depicted in red is measured by Brillouin light scattering metrology. The bottom horizontal axis gives the power scaling factor whereas the top horizontal axis gives the actual power. We add black (red) error bars to indicate standard deviations of the calculated CTE (Young’s modulus). The CTE decreases (Young’s modulus increases) with the laser exposure power. Both variations are approximately linear.

Figure 3. **Functional stacks fabricated by gray-tone lithography.** (a) (c) Optical micrographs and (b) (d) SEM images. Each stack is composed of five elements. The samples are composed of two

constituent components fabricated with a single photoresist but two different laser exposure powers. Differential shrinkage during development leads to pre-bending of the bi-layer beams, further leading to rotation (translation) of the stack shown in the panels.

Figure 4. **Temperature-dependent measurement of the fabricated stacks.** (a) (c) Dependence of motional amplitudes of the stacks with the thermal gradient for rotation and translation, respectively. The plots show a symmetric, linear and reversible amplitude response. (b) (d) Cyclic stability of the structures for rotation and translation, respectively, where temperatures are switched between 25°C (marked in blue) and 45°C (marked in red). The error bars (marked in black) indicate the difference between experimental and numerical results. Note that the translational displacements in panels (c-d) are normalized to the initial non-heated stack length in the z-direction. (e) (f) The specific work (i.e., the work normalized to the mass of the structure) and the actuation motion of the elements under thermal stimuli are plotted versus the normalized load and represented in analogy with Hooke’s springs shown in the insets. Loads M_0 and M_1 have been normalized by the mass of the rotational element (2.5×10^{-10} kg) and translational element (2.1×10^{-10} kg), respectively. A linear relationship between displacements and external loads is observed in both cases, suggesting that the elastic limit is not reached.